Hematite surfaces: Band bending and local electronic states

S. Rostami [ORCID],[*] N. Seriani, and R. Gebauer

The Abdus Salam International Centre for Theoretical Physics, Strada Costiera 11, 34151, Trieste, Italy

Hematite is a promising material for photoelectrochemical water splitting applications and understanding the complete mechanism of water oxidation reaction close to its surfaces is of great importance. Herein, we present a theoretical investigation of the electronic states of nonstoichiometric hematite(0001) films in the presence of absorbed H on the surfaces, as well as Ti doping. The calculations, performed at the DFT $+ U$ level, indicate that iron can appear in different oxidation states, from Fe^{2+} to Fe^{4+} and Fe^{5+} in the vicinity of impurities or surfaces. The electron and hole distributions in hematite slabs could control the bending and local state of valence and conduction bands. The projected density of states in different atomic positions shows an upward band bending close to the surfaces, which varies with the number of absorbed H or with Ti doping. In the dark, the width of the depletion layer is computed as less than 12 Å for neutral slabs, while adding excess electrons expands it to involve more atomic layers, depending on the number of absorbed H on the surface. In the neutral slabs in the presence of H, we obtain an upward band bending of 0.18, 0.42, and 0.24 eV by increasing the number of H from one to three on each side, respectively. The evolution of bands in neutral slabs, with/without Ti doping, occurs in a few layers in nearby the surface and also Fe with an oxidation state rather than Fe^{3+}. According to our results, doping Ti creates a polaron and locally affects the band structure. In the charged surface with excess electrons, a metallic behavior is observed on the surface and a large band bending in the middle layers. This work shows that a substantial upward bending of the bands in hematite can exist even at neutral surfaces in contact with a vacuum.

I. INTRODUCTION

Hematite (α-Fe_2O_3) has great potential in photoelectrochemical (PEC) water splitting applications used for solar energy conversion [1]. Having a band gap $\sim$2.0 eV for adsorbing visible light and excellent stability in photochemical reactions makes hematite a suitable material for PEC water splitting. Due to the importance of this iron oxide, many experimental and theoretical works have been performed to understand its properties [2,3]. However, its efficiency is limited by the high recombination of photogenerated electrons and holes in surface and bulk. Despite vast studies on this material, still a complete mechanism of water oxidation reaction on a hematite surface and migration or recombination of photogenerated charge carriers through its bulk are not clear; understanding of these processes is necessary to improve the efficiency of PEC cells.

Extensive theoretical studies attempted to understand the chemical reactions and the electronic properties of different α-Fe_2O_3 surfaces [4–10]. Cutting the rhombohedral structure of hematite along the (0001) axis generates a stable surface. The (0001)α-Fe_2O_3 slabs can be found in various terminations and stoichiometries, each of them behaving differently in adsorption of gases, such as O_2, H_2, and H_2O, in a water-splitting process [5,7–9].

A stoichiometric slab exhibits the formal oxidation states of Fe^{3+} and O^{2-}. On the other side, in nonstoichiometric slabs Fe can be present in different oxidation states, which lead to the generation of extra holes in the top surface layers. Theoretical and experimental studies confirmed that in hematite surfaces, Fe can be observed in different oxidation states 3+, 4+, and 5+ during the reaction [11–16]. The surface-trapped hole densities play an important role in water-splitting reactions through increasing the concentration of electron acceptors on the surface. For example, in the reaction path of water oxidation on a hematite surface, on pure O-terminated slabs, two Fe on the top layer can appear in +4 and +5 states which employ three surface-trapped holes for receiving electrons and accepting H or OH bonds on the surface [11,12].

To enhance the performance of hematite, it is commonly doped with the +4 valence state elements such as Ti, Zr, and group IV elements (Si, Ge, or Si) [17–24]. Substituting one +4 valence state element with Fe introduces a charge transfer from that element to a surrounding Fe which becomes Fe^{2+}. Titanium doping is one of the most effective modifications of hemtite. In experimental studies of nanostructures and thin films of Ti-doped hematite, it is observed that, depending on the dopant concentration, the performance of photocurrent density would enhance relative to pure hematite due to increasing the band bending and decreasing the electron/hole recombination rate [22,25–28]. For instance, using nanostructured films can increase photocurrents approximately by 220% [25].

———————
*samare.rostami@gmail.com

104604-1

Dopants can occupy different sites in a slab which affects the electronic states of the surface. In a combination of experimental and theoretical studies on surface reconstructions of pure and Ti-doped surface α-Fe$_2$O$_3$($1\bar{1}002$), they determined that by substituting Fe with Ti, a nearby Fe should be in a charge state of 2+ on which the polaron is localized [29]. In their slabs, the Ti is energetically more stable when located in the second top layer in zigzag rows, in agreement with the experimental observations. Recently, codoping of +4 cations together with (-1 or -3) anions or oxygen vacancies were shown to be effective. Combinations such as (N/F,Ti:Fe$_2$O$_3$) [30,31] or Ti:Fe$_2$O$_3$ codoped with O vacancy [32] enhance the current density approximately two to three times with respect to the values obtained for singly doped hematite with Ti.

Since the first theory of band bending in semiconductors at interfaces by Schottky and Mott, many studies tried to analyze and understand the photoexcitation process by their model. An increased band bending potential in the surface layer would help the excited electron and hole separation. For an n-type semiconductor, the Fermi level shift toward the conduction band (C_B) and an upward band bending, from bulk to the surface, occurs on top of the valence band (V_B). Under applied bias voltage V, the width of the depletion layer (space charge region) can be calculated as $W_{sc} = [2\epsilon_0\epsilon_s(V - V_{fb})/(qN_d)]^{1/2}$, where ϵ_0 and ϵ_s are the dielectric constant of the vacuum and the semiconductor, respectively, N_d is the concentrations of donor, and q is the charge of the electron. In the experimental results, these values would be computed by measuring the flat band potential V_{fb} and density of charges. For pure hematite, the V_{fb} is reported to be 0.4 to 0.5 V [33,34], resulting in a the depletion layer of about 24 nm in dark condition [34]. At an applied bias of 1.23 V versus RHE, which is a standard reduction potential for water splitting under illumination, the W_{sc} would increase to over 30 nm (less than 100 nm) [5,12,15,18,33–36]. The band bending is calculated to be between 0.1 to 1 eV under different bias potential. In a previous theoretical study on Fe-terminated stoichiometric hematite [5], the band bending was calculated as 0.14 and 0.49 eV for the pure surface and with adsorbed OH, respectively. While in the dilute-doped hematite the flab band is measured similar to pure condition, [16,18,34,35,37] the W_{sc} is reported to decrease to 3.8 nm (6.7 nm) for 5% Ti doping under dark (illuminated) condition and 8 nm for 3% Sn doping [18,34].

Herein, we presented a theoretical DFT $+ U$ study on pure and Ti-doped Fe$_2$O$_3$(0001) film with varying absorbed H on the surfaces. For different surface conditions with/without excess charges, the electronic states of different atoms are investigated by looking at atomic magnetic changes. By plotting the projection density of states of all atoms in their atomic positions, we demonstrate the localized states close to impurities and also the band bending in the top surface layers.

II. COMPUTATIONAL DETAILS

In this work, the density functional theory (DFT) calculations are performed within the framework of the generalized gradient approximation (Perdew-Burke-Ernzerhof) GGA(PBE) $+ U$ [38,39] formalism as implemented in the QUANTUM ESPRESSO software [40]. Ultrasoft pseudopotentials with a wave-function energy cutoff of 40 Ry and a charge density cutoff of 480 Ry are chosen to converge the total energies to within 1 meV/atom. Aligning to previous studies, we use a Hubbard $U = 4.2$ eV for iron, which leads to a band gap of 2.0 eV in hematite [7–9].

The α-Fe$_2$O$_3$ bulk has a corundum-like structure in a hexagonal unit cell containing six Fe$_2$O$_3$ formula units (30 atoms). By optimizing the hematite structures using an antiferromagnetic arrangement for Fe-bilayers [41], the lattice constants of $a = 5.11$ and $c = 13.94$ Å is obtained (experimental results: $a = 5.04$ and $c = 13.75$ [42]).

The most stable surface of hematite, Fe$_2$O$_3$(0001), can be generated in different oxygen or iron terminations. Some properties of these different terminations were studied in previous works [7]. Here we focus on an oxygen-terminated surface with three oxygen on each side of the slab. This nonstoichiometric slab contains a formula unit (Fe$_2$O$_3$) for each Fe-bilayer plus three extra O's to terminate with oxygen at each side. Due to the antiferromagnetic order for Fe-bilayers, the total magnetization of the slab would be computed as 0 and 4 μ_B/cell by considering even and odd bilayered systems, respectively. However, we calculated that the total density of states of electrons close to the surfaces does not change significantly between even and odd bilayered systems. The only difference is a change in the direction of spin channels (up/down) in the surface layers.

The slabs are built with a (1×1) surface cell in a different number of bilayers. A vacuum larger than 25 Å between slabs and their periodic images is considered. To sample the Brillouin zone for all slabs, a $4 \times 4 \times 1$ k-point grid is chosen. Four different surfaces are generated by presenting H on each termination: pure slab (S) and with one, two, and three absorbed H, called H-S-H, H2-S-H2, and H3-S-H3, respectively, as shown in Fig. 1. A fully atomic relaxation is employed to find the optimized surfaces.

The charges slabs are generated by adding one extra electron per each side of the slabs with all four mentioned surfaces with 23 Fe-bilayers. For considering the Ti-doped slabs, we swap two Fe by two Ti symmetrically in different layers of the slabs with 19 Fe-bilayers (3H-S19-3H and 2H-S19-2H).

III. SLABS WITH/WITHOUT HYDROXYL GROUPS

We investigate the electronic properties of charge-neutral slabs with the four mentioned surfaces (S, H-S-H, 2H-S-2H, and 3H-S-3H). The convergence test on band bending, employing slabs with different thicknesses, from 7 to 13 Fe-bilayers, shows that convergence can be achieved in slabs with thicknesses larger than 11 bilayers. By increasing the thickness, in the middle of the slab we should have a bulk behavior with a band gap of 2.0 eV.

In this work, we report the results of 12-bilayered systems. In the pure 12-bilayered slab (S12) and all its surfaces containing absorbed H, we have a mirror symmetry for atomic magnetization, which leads to a total magnetization equal to zero. For odd bilayers, the total magnetization would not vanish in such a way that in pure slab it should be 4 μ_B/cell and it increase by one per each H in the system. Therefore, for 13 bilayered slabs, the total magnetization accepts the values
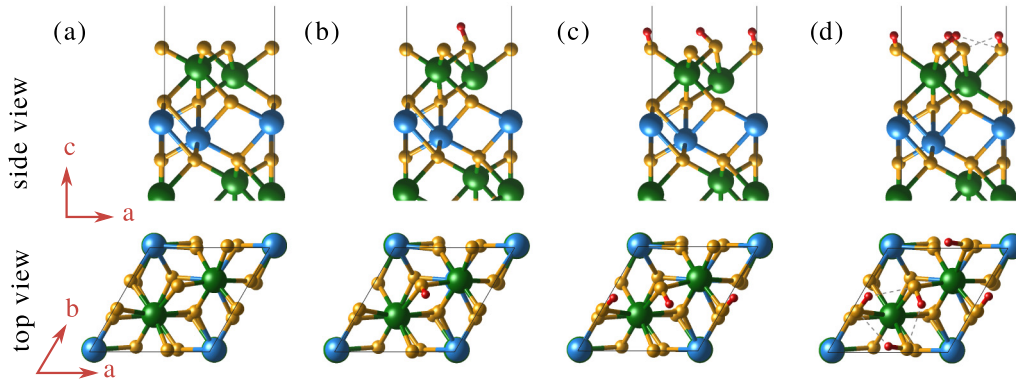
FIG. 1. Top and side views of the O-terminated slab models with different hydroxyl groups. (a) pure slab (S), (b) H-S-H, (c) 2H-S-2H, and (d) 3H-S-3H. In all the figures, green, blue, orange, and red balls indicate Fe (spin-up), Fe (spin-down), O, and H, respectively.

from four to eight by two for $S13$ to 3H-$S13$-3H. However, this magnetization would not change the behavior of states close to the surfaces. For a comparison, in the Supplemental Material [43] the results of 13 layers are presented. For case of $S12$, as shown in Fig. 2, we have a perfect O -terminated surface in both sides with a thickness of 27.69 Å.

For all surfaces, the atomic positions are completely relaxed. In Fig. 2, the results of the density of states (DOS), projected density of states (PDOS), and electronic states of different layers are illustrated. In all DOS plots, a symmetric behavior for spin-down and spin-up channels is observed. The plots show the place of local states between conduction and valence bands (C_B and V_B, respectively) are different. For digging into the occupation of states in the position of slabs, the projection of particular orbitals of each atom are plotted in their z coordination. In PDOS figures, we plot the sum of the values of spin-up and -down channels for $3d$ iron orbitals and $2p$ oxygen orbitals. For better visualization, just the values
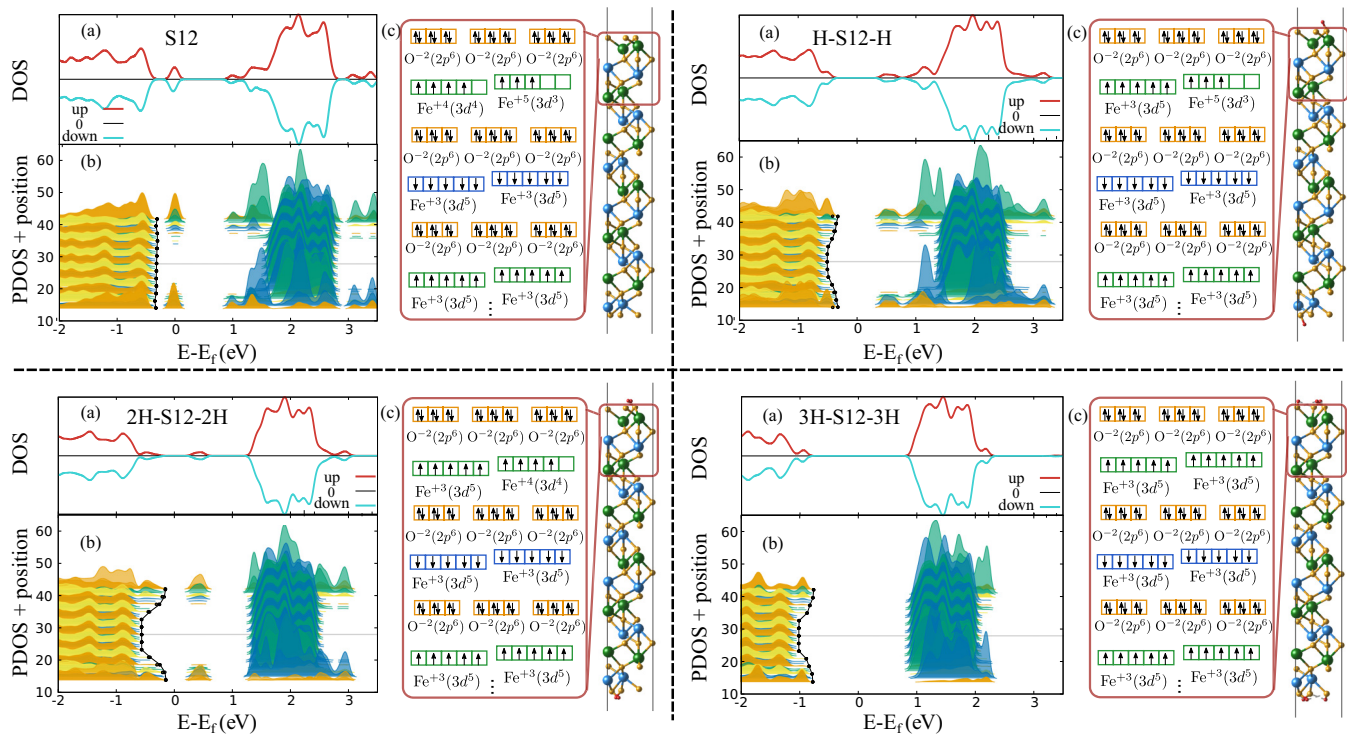

FIG. 2. Characteristic of states in O-termination hematite slabs, S12, H-S12-H, 2H-S12-2H, and 3H-S12-3H. (a) The total density of state in which positive and negative values show the spin-up and the spin-down channel, respectively. (b) Projected density of states is plotted for all atomic orbitals. For more visibility, all PDOSs are shifted by corresponding atomic position in a nonperiodic direction. The energies for both DOS and PDOS are shown with respect to the Fermi level. Here, the PDOS values are plotted as a sum of the spin-up and spin-down channels and the values less than 0.01 are ignored. The green and blue curves indicate the orbital of Fe ($3d$) with different spin orientations (up and down, respectively). The yellow and orange curves identify the O ($2p$) orbitals and different colors are chosen to separate different O-bilayers. The black line and dots show the top of the valence band of each O ($2d$) orbital. (c) Arrangements of the electrons in the orbitals of the first six O/Fe bilayers. In panel (c), green, blue, orange, and red balls indicate Fe (spin-up), Fe (spin-down), O, and H, respectively.

TABLE I. Magnetic moment per atomic site (μ_B/atom) obtained from Mulliken analysis for the atoms in the surface and middle layers of the S12 films with different hydroxal terminations are listed. The band bending (BB) is reported according to the variation of the top of valence bands as shown in Fig. 2.

Atom	$S12$	H-$S12$-H	2H-$S12$-2H	3H-$S12$-3H
O1	0.00	0.11	0.09	0.10
O1	0.00	0.09	0.05	0.10
O1	0.00	0.00	0.08	0.10
Fe1	2.46	2.46	3.15	3.85
Fe1	3.34	3.58	3.60	3.84
O2	−0.12	−0.05	−0.04	0.00
O2	−0.12	−0.05	−0.02	0.00
O2	−0.12	−0.04	−0.02	0.00
Fe	3.59	3.56	3.58	3.81
O	0.00	0.00	0.00	0.00
Total:	0	0	0	0
BB(eV)	0.00	0.18	0.42	0.24

larger than 0.01 are presented and also the values of O and Fe orbitals are plotted in different colors.

In bulk hematite, all the irons are equivalent with five single electrons in their $3d$ orbital and the same absolute magnetization. By a Mulliken analysis, for all irons, we have a $\mu = 3.81$ Bohr magnetons with a different sign due to the antiferromagnetic ordering. The construction of slabs and also the addition of hydroxyl groups or dopants would change the oxidation of atomic states and accordingly the atomic magnetization. Therefore, by checking the density of states and comparing the magnetization, we could be able to trace the position of electrons in atomic orbitals. In Table I the Mulliken analysis of S12 with different surfaces is listed. In our evaluation, removing/adding one μ_B/cell electron from/to a Fe($3d$) orbitals will change the value of magnetization by almost 0.5 μ_B/cell.

By analyzing the magnetization, as reported in Table I, we detect different atomic states in the surface and intermediate layers. In S12, H-$S12$-H and, 2H-$S12$-2H, the absolute values of magnetization in deep layers are computed to be of ∼3.56 and 0.00 μ_B/cell for all Fe³⁺($3d^5$) and O⁻²($2p^6$), respectively. While, the atomic magnetization of elements in 3H-$S12$-3H behaves like the bulk of hematite (3.81 and 0.00 μ_B/cell).

For the pure slab, S12, the values of magnetization of two Fe in the top bilayer are changed to 2.46 and 3.34 that we refer them as Fe⁵⁺($3d^3$) and Fe⁴⁺($3d^4$), respectively. However, we cite 3.34 μ_B/cell to Fe⁴⁺ by leniency since the difference of it with the value of Fe³⁺ is ∼0.2 μ_B/cell, which is smaller than our criterion of ∼0.5 μ_B/cell. Moreover, some changes in the magnetization of O atoms in the second top layer of O is obtained. PDOS figures (S12 in Fig. 2) shows the localized states close to V_B continued in a few surface layers in which the accommodation of charge distribution on O($2p$) states of the first O-layer is higher than other atomic states in the deeper layers. In our definitions [5], the band bending is identified by the evolution of the top of the V_B of all individual atoms, from the surface through the slab. We exclude the localized states from considering the V_B. In this way, for the pure hematite

slab (S12), we have a flat valance band as shown by a black line and points in Fig. 2(b).

Adding H on the surfaces varies the population of electrons in Fe orbitals. In Fig. 2, the characteristic of states of S12 with one H on each side (H-$S12$-H) is illustrated. The magnetization in Table I determines the presence of Fe⁵⁺ and Fe³⁺ in the first Fe-bilayer. The calculations show that Fe⁵⁺ and Fe³⁺ are more favorable than two equivalent Fe⁴⁺. DOS and PDOS display that the V_B would be affected by the presence of H on the surface, which introduces a band bending in a few layers close to the surfaces. The results show a band bending of 0.18 eV with a thickness of almost 11.5 Å. Also, a local change appears in the C_B. In 2H-$S12$-2H (Fig. 2), we could see band bending and also a local states between V_B and C_B. In a thickness of 9.2 Å, the bands are changed by 0.42 eV.

Finally, in a fully hydroxylated surface (3H-$S12$-3H), all irons occupy five electrons in their $3d$ orbital like in a bulk system and there are no extra electrons and holes. For this case, the magnetization of all Fe and O are almost similar to bulk values (∼3.81 and 0.0 μ_B/cell) and only there are small changes in surface O's by 0.1μ_B/cell. From the PDOS, five first layers are involved in the band bending of 0.24 eV with 11.5 Å width. All of these results are also valid for S13 and its different surfaces containing absorbed H. For the odd number of bilayers, we do not have a symmetric magnetization. As a consequence, Fe with spin up and down have different values for magnetization. For example, if we determine the first and last bilayer with spin up, for S13, H-$S13$-H, and 2H-$S13$-2H, irons with spin up get values about ∼3.58 similar to the S12 model while irons with spin down prefer to reserve the bulk magnetization ∼3.81 μ_B. However, this variation would not affect the behavior of band bending and the density of states.

In conclusion, we cannot find any special trend for the behavior of bands in the surface layers. The band bending is highly dependent on the occupation of atomic orbitals and terminations of slabs.

IV. CHARGED SLABS

In this section, we analyze the charged cells with different surfaces. To generate the charged slabs, two excess electrons (one per each side) are added to our surfaces and the atomic positions are optimized. In QUANTUM ESPRESSO, when adding excess charges, a uniform background ("jellium") is applied to neutralize the total charge of the cell. These background charges should not change the interpretation of charge accommodations in the system. To check the affect of jellium background charges, we vary the size of the supercell, increasing the size of the vacuum between periodic images of the slab. At constant charge on the slab, this leads to a variation of the background charge density. In the limit of a very large vacuum region, the jellium density tends to zero. The results of this test are presented in the in the Supplemental Material [43]. The results show that varying the vacuum size does not change the results significantly and small ionic realizations lead to a noise that is less than 1%.

In even-bilayered systems, the magnetization is always zero due to the symmetries. But in odd-bilayered systems, the story is different since the total magnetization does not vanish. For our odd-bilayered systems, we expect that by adding

TABLE II. The magnetic moment per atomic site (μ_B/atom) obtained from Mulliken analysis for charged slabs with two excess electrons. The results for the surface and the middle layers of the different S23 with different hydroxyl terminations are listed. The magnetic moment of iron with spin-up, Fe (u), and spin-down, Fe (d), channel are reported separately in the central layers. For comparison, The total magnetization of neutral slabs is also presented. The BB is reported according to the variation of the top of valence bands as shown in Fig. 4.

Atom	$S23$ ($2e$)	H-$S23(2e)$-H	2H-$S23(2e)$-2H	3H-$S23(2e)$-3H
O1	0.09	0.16	0.29	0.09
O1	0.09	0.06	0.07	0.09
O1	0.09	0.05	0.08	0.09
Fe1(u)	2.47	3.02	3.55	3.84
Fe1(u)	3.71	3.58	3.66	3.81
O2	−0.14	−0.07	−0.04	0.03
O2	−0.14	−0.05	−0.04	0.03
O2	−0.14	−0.05	−0.03	0.03
Fe2(d)	−3.78	−3.76	−3.77	−3.78
Fe2(d)	−3.78	−3.77	−3.78	−3.56
Fe(u)	3.78	3.59	3.65	3.78
Fe(d)	−3.78	−3.76	−3.77	−3.78
O	0.00	0.00	0.00	0.00
Total:				
Neutral	4	6	8	10
Charged	5.42	7.27	9.23	11.12
BB (eV)	1.24	1.95	1.85	0.70

two electrons, the total magnetization of our uncharged slabs changes by 2 μ_B/cell. Although the results for odd-bilayered slabs, as listed in Table II for 23-bilayered systems, show that we could obtain values lower than our assumption.

For the charged hematite with odd-bilayered slabs, we use constraints on the magnetization to bring the system close to the local minimum with the desired magnetization. Once the system is close to convergence, the constraints are eliminated.

The saturation of band bending takes place at the thickness of 53.55 Å obtained for the 23-bilayered slab ($S23$).

The profile of the planar and macroscopic average electrostatic potential in Fig. 3 illustrate a flat potential in the vacuum and a symmetric potential close to the surfaces. The planar average figure shows that the hydrogenation of surface changes the potential at the interface, which acts like a barrier. The flat potential in the center of the slab confirms that the variations of electronic states and potential at the surfaces do not effect the inner layers. We thereby confirm the convergence of the results with respect to the thickness of the slabs.

In Fig. 4, the specifications of atomic orbitals and density of states of four charged slabs, $S23(2e)$, H-$S23(2e)$-H, 2H-$S23(2e)$-2H, and 3H-$S23(2e)$-3H are presented. By evaluating the atomic magnetization reported in Table II we find that, except 3H-$S23(2e)$-3H, the extra electron fills the Fe($3d$) orbitals in the first bilayer.

In $S23(2e)$, the surface layers contain both Fe^{3+} and Fe^{5+} and we have local states close to the valence bands like the neutral slab $S12$. A large BB around 1.24 eV appears by adding this extra electron, which extends until the middle of the slab as shown in Fig. 4.

At a first view of DOS figures for H-$S23(2e)$-H and 2H-$S23(2e)$-2H (Fig. 4) one can notice that the slabs become metallic and the band gap disappears. However, projecting the density of states indicates that in H-$S23(2e)$-H, this metallic behavior just involves the surface layers, while the deep layers remain in semiconductor condition with a band gap of ∼1.8 eV. We could not define a certain band bending for this case since the band on the surfaces are continuous.

For 2H-$S23(2e)$-2H, even on the surface we have a small gap. However, the bands are distorted somehow that their energy of V_B at the surface reaches the energy of C_B in the middle of slabs. In this way, the total DOS would detect a continuous band without any gap. In fully hydroxylated systems, 3H-$S23$-3H, there is no trapped hole on the surface and all Fe is in the same oxidization of +3 with a half-filled $3d$ orbital. The extra electron in 3H-$S23(2e)$-3H, should be occupied in the $3d$ orbital of Fe to produce Fe^{2+} with paired electrons. The value of magnetization in Table II illustrates a change on magnetization and generation of one Fe^{2+} in the second Fe-bilayers. Also, the blue sharp peak in PDOS figure confirms that the electron highly localizes in the $3d$ orbital of one Fe in the second bilayer. A band bending of 0.7 eV is computed for this slab.
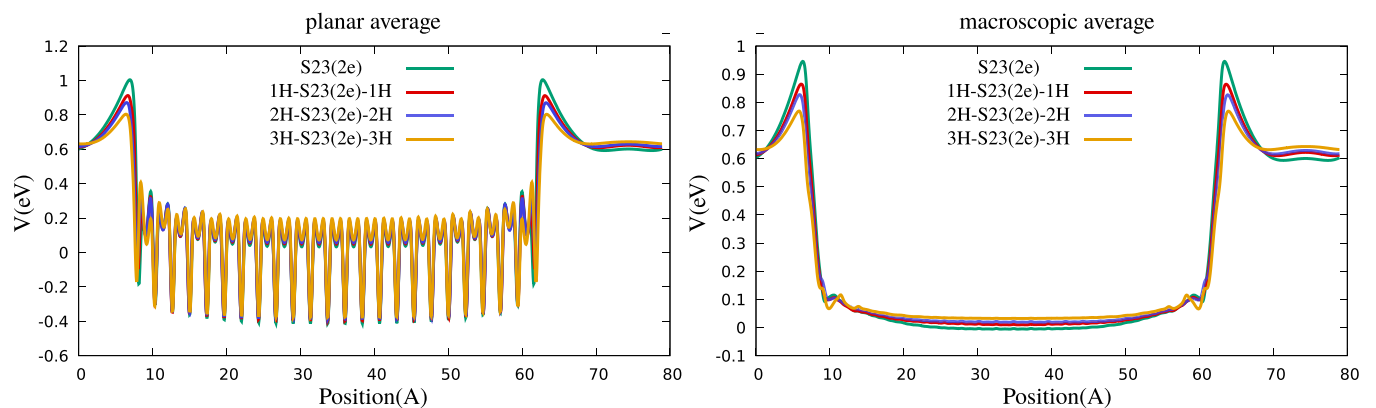

FIG. 3. Planar and macroscopic averages of the electrostatic potential across the 23-bilayered slabs with two excess electrons, $S23$ ($2e$), and different hydroxal terminations.
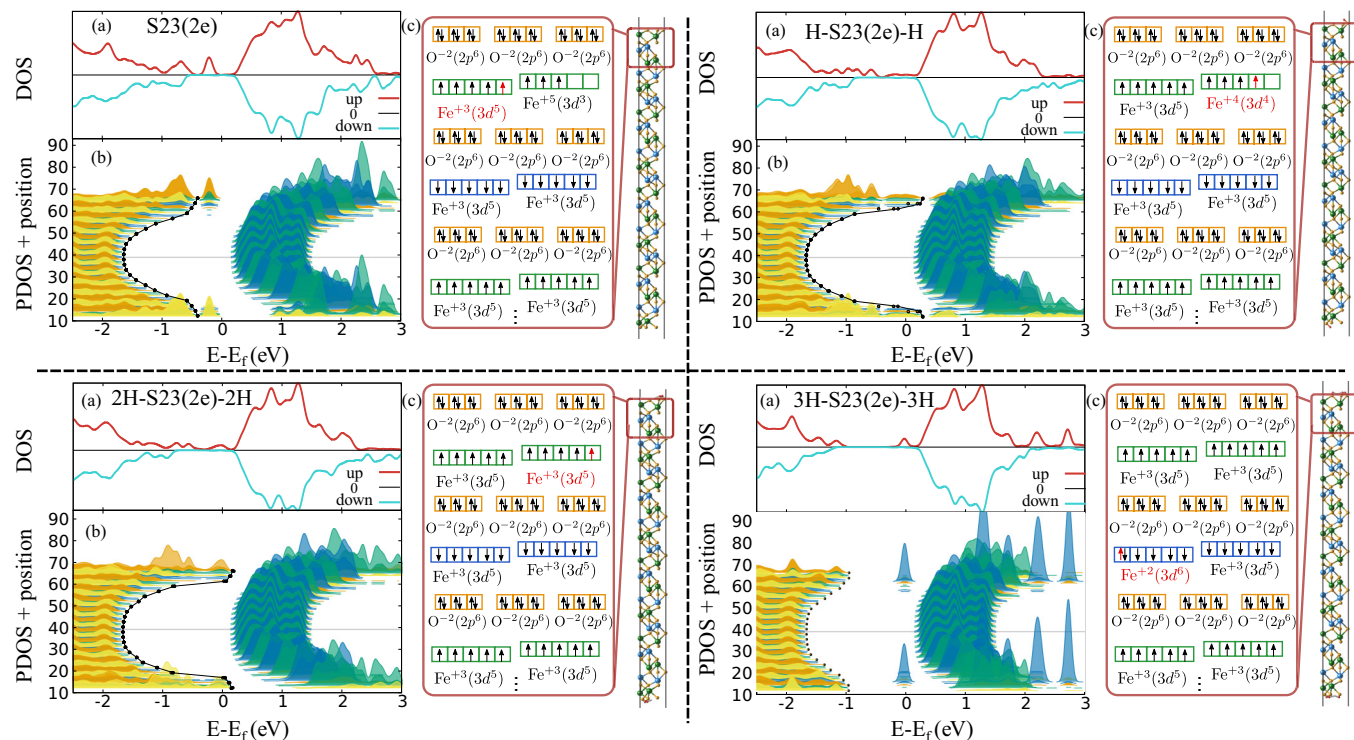
FIG. 4. Characteristic of states in S23 (2e), H-S23 (2e)-H, 2H-S23 (2e)-2H, and 3H-S23 (2e)-3H. The same conventions are used as in Fig. 2. The red arrow in panel (c) indicates the position of excess electron in atomic orbital.

V. TI-DOPED SLABS

To understand the charge distribution of Ti-doped systems we substitute two Fe in different positions with Ti by considering the symmetry of the slab. we employed 2H-$S19$-2H and 3H-$S19$-3H surfaces which generate 5% Ti-doping systems. Total magnetization depends on the position of Ti and the accommodation of electrons in the lattice since our slab contains odd-bilayered slabs, the total magnetization of a system without Ti would be 8 and 10 μ_B for 2H-$S19$-2H and 3H-$S19$-3H, respectively.

Using different initial configurations, generated by slightly changing the position of atoms in neighboring Ti and also surface layers, determine that for our cases, the electron of Ti($3d^1$) would rather transfer to the first neighboring bilayered and mostly to the closest Fe. If the electron of Ti($3d^1$) transfers to a Fe^{3+} in the alternative bilayer to generate a Fe^{2+}, the total magnetization of undoped slabs would change by $+/-4 \mu_B$ for each added Ti. The situation would be different if the electron moves to the Fe in the same bilayer of Ti, or if it goes to the Fe with different oxidization and it could be computed by summing up the spin of unpaired electrons for all elements.

In Fig. 5, the characteristic of electronic states of Ti-doped slabs, 2H-S19(2Ti)-2H and 3H-S19(2Ti)-3H, are presented. In our notation, (Lm_n) indicates that the Ti located in the mth with bilayer respect to the surface. The position of atoms in a bilayer is shown by n which is equal to 1 for the position closer to the surface, and 2 for the farther one.

In 3H-$S19$-3H, all Fe presented in the surfaces or deep layers are in the equivalent state of 3+ and adding Ti could generate Fe^{2+} in different positions depending on the place of Ti. In all cases, the PDOS indicates the localized states (sharp blue/green peaks) on the center of Fe^{2+} which continues slightly to close neighboring atoms. For 3H-$S19$[2Ti($L1_2$)] − 3H and 3H-$S19$[2Ti($L2_2$)] − 3H in which the electron is transferred to the deeper layers, we could see an almost the flat band all layers and just on the surface, a very small downward band bending is illustrated. In 3H-$S19$[2Ti($L2_1$)]-3H, where Ti takes place in ($L2_1$), the electron lies on the Fe in ($L1_2$), we have a combination of Fe^{2+} localized peaks with continuous states which shift the V_B by 0.80 eV within a 7 Å width, and for the rest of the middle layers, the the flat band is observed.

In 2H-$S19$-2H, one surface trapped charge corresponding to a Fe^{4+} exists in ($L1_1$), which would be a suitable host for the free electron of Ti($3d^1$). For the cases the Ti located in ($L1_2$), ($L2_1$), and ($L2_2$), the electron would transfer to the surface turn Fe^{4+} to a more stable state of Fe^{3+}. For the layers deeper than three, the electron would move to just the nearest bilayer and we could not manage to locate the electron in the top layer. 2H-$S19$[2Ti($L1_2$)]-2H display a totally flat band. In this case, all the iron are in the (3+) state and a total magnetization equals zero. The variation of the V_B is 0.83 and 1.16 eV close to the 2H-$S19$[2Ti($L2_1$)]-2H and 2H-$S19$[2Ti($L2_2$)]-2H surfaces, respectively, affected a width of 7 Å from the surface. The 2H-$S19$[2Ti($L3_2$)]-2H we determine distinguished band bending and localized Fe^{4+} states. By moving Ti to the deeper layers ($L9_2$) in Fig 5, the band bending on the surface would converge to results computed for undoped slabs and some localized states disturb the bands in the vicinity of the dopant.
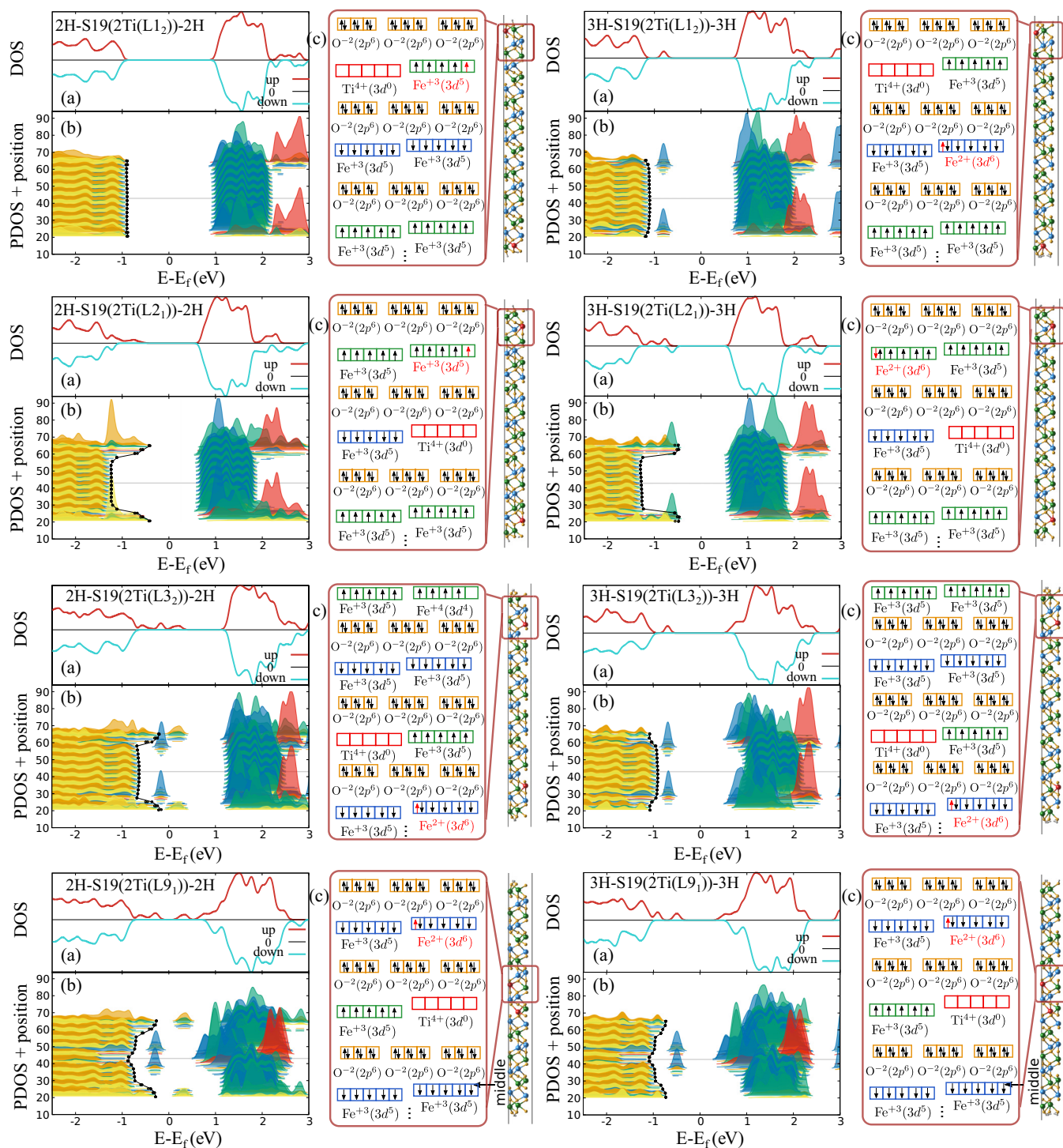
FIG. 5. Characteristic of states in 2H-S19-2H and 3H-S19-3H with the presence of Ti-doping in different positions, 2H-S19[2Ti(L1$_1$)]-2H, 2H-S19[2Ti(L2$_1$)]-2H, 2H-S19[2Ti(L3$_2$)]-2H, 2H-S19[2Ti(L9$_1$)]-2H, 3H-S19[2Ti(L1$_1$)]-3H, 3H-S19[2Ti(L2$_1$)]-3H, 3H-S19[2Ti(L3$_2$)]-3H, and 3H-S19[2Ti(L9$_1$)]-3H. The same conventions are used as in Fig. 2. In panel (c), green, blue, red, orange, and gray balls indicate Fe (spin-up), Fe (spin-down), Ti, O, and H, respectively. The red curves in panel (b) indicate the Ti(3d) orbitals.

As listed in Table III, energetically Ti would rather place in the first layer for both surfaces. However, the lowest energy in a fully hydroxylated surfce belongs to 3H-S19[2Ti(L10)]-3H when two Ti are placed exactly in the middle of the slab in the same layer. To conclude, the results show that in all cases, the dopants can generate some localized states, which,

however, affects the environment only in the neighborhood of the dopant. In Fig. 6, the band bending of 3H-S19(2Ti)-3H and 2H-S19(2Ti)-2H systems is illustrated. The band bending is converged at surface layers when Ti is far from the surface. For Ti in the first layers, we could not find a correlated behavior in the results.

TABLE III. The total energy of Ti-doped 2H-S19-2H and 3H-S19-3H films. The energies are reported in eV/cell with respect to the energy of 2Ti($L1_2$) slabs. The BB is reported as the energy difference of the surface O atoms and fifth O layer (gray vertical line in Fig. 6).

Atom	2H-S19-2H		3H-S19-3H	
	Energy	BB	Energy	BB
2Ti($L1_2$)	0.000	0.02	0.000	−0.07
2Ti($L2_1$)	1.002	0.83	0.083	0.78
2Ti($L2_2$)	1.525	1.15	0.075	−0.09
2Ti($L3_2$)	2.660	0.50	0.040	−0.15
2Ti($L9_1$)	3.082	0.44	0.402	0.22
2Ti(10)	2.480	0.44	−0.193	0.24

VI. CONCLUSION

In summary, within the framework of DFT + U, we investigated the electronic structure and band bending on α-Fe$_2$O$_3$(0001) films with four different surface conditions. The O-terminated surface is considered in presence of adsorbing H atoms as well as Ti impurity. During a water oxidation reaction mechanisms, as indicated in the experimental analysis [11,12,44], a different number of OH sites can be presented on the surface of hematite, which varies the amount of the electrons and holes close to the surface. Our results show that the behavior and bending of the valence and conduction band is highly dependent on the situation of electrons and holes in surface layers, which affect the diffusion of charge carriers during the water-splitting reaction path.

Considering the different surfaces and Ti-doping, Fe can appear in oxidization states in the range from 2+ to 5+. The band bending, depending on the surface condition, changes from 0.0 to 0.42 eV for neutral films and increases by adding excess electrons. In a charged slab, H-S23(2e)-H, projection of the density of states illustrates a metallic behavior on the top surface layers followed by a semiconductor situation in the middle of slab. By doping the slabs with Ti, Fe^{2+} would be introduced in the vicinity of dopant, which causes the appearance of localized states at its position. When titanium is located far from the surface, the band bending approaches the values computed for the undoped films. Except the charged slabs, the width of band bending equal to less than 12 Å. This work shows that even neutral surfaces in contact with a vacuum can display a substantial upward bending of the bands in hematite. These results can help rationalize the behavior of electrons and holes at surfaces of hematite.
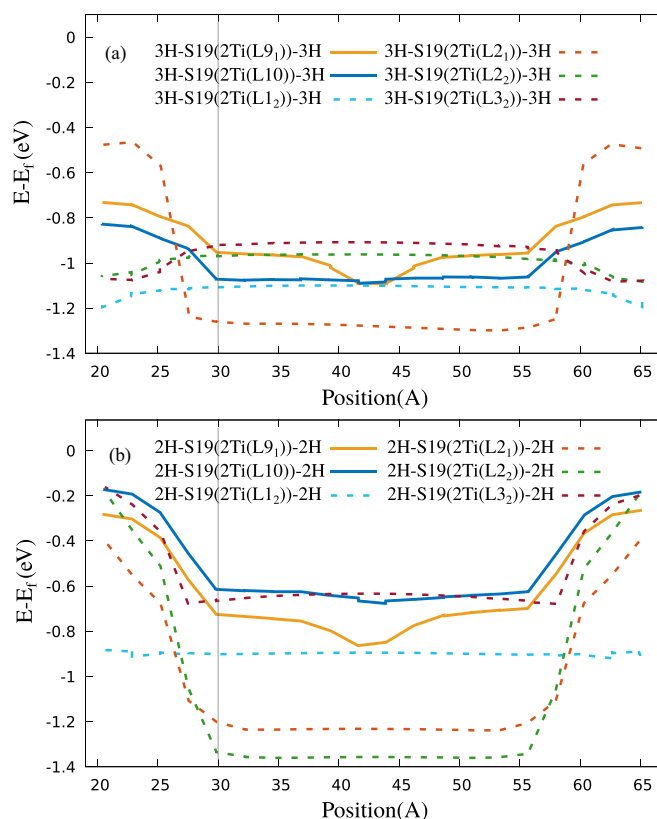

FIG. 6. Top of the valence band with respect to the Fermi level vs the positions of the oxygen atoms in Ti-doped 3H-S19-3H and 2H-S19-2H slabs in (a) and (b) panel, respectively. Dashed lines show the slabs in which Ti is occupied in bilayers close to the surface. Solid lines indicate the slabs with Ti doping in the central bilayers.

Summarizing, we showed that band bending can be present even at the surface of hematite in contact with a vacuum, and that its value is influenced by the adsorption of neutral species, such as atomic hydrogen. In the real system in contact with an electrolyte, different states of hydrogenation of the surface may exist under reaction conditions, as illumination provides a driving force for surface deprotonation. Moreover, our calculations show that titanium doping influences the band bending only if the Ti impurity is located in the immediate vicinity of the surface. Finally, additional electrons have a stronger effect on the band bending than any of the other perturbations. Such rich phenomenology in the absence of an electrolyte has been so far overlooked and can provide a starting point to investigate and a reference to interpret the more complex behavior of the hematite surface in contact with an electrolyte.

[1] K. Sivula, F. Le. Formal, and M. Gratzel, ChemSusChem **4**, 432 (2011).

[2] N. Seriani, J. Phys.: Condens. Matter **29**, 463002 (2017).

[3] A. G. Tamirat, J. Rick, A. A. Dubale, W.-N. Su, and B.-J. Hwang, Nanoscale Horizons **1**, 243 (2016).

[4] S. M. Souvi, M. Badawi, J.-F. Paul, S. Cristol, and L. Cantrel, Surf. Sci. **610**, 7 (2013).

[5] P. A. Delcompare-Rodriguez and N. Seriani, J. Chem. Phys. **155**, 114701 (2021).

[6] R. B. Wang and A. Hellman, J. Chem. Phys. **148**, 094705 (2018).

[7] M.-T. Nguyen, N. Seriani, and R. Gebauer, J. Chem. Phys. **138**, 194709 (2013).

[8] M.-T. Nguyen, N. Seriani, S. Piccinin, and R. Gebauer, J. Chem. Phys. **140**, 064703 (2014).

[9] M.-T. Nguyen, N. Seriani, and R. Gebauer, Chem. Phys. Chem. **15**, 2930 (2014).

[10] P. Liao, J. A. Keith, and E. A. Carter, J. Am. Chem. Soc. **134**, 13296 (2012).

[11] C. A. Mesa, L. Francàs, K. R. Yang, P. Garrido-Barros, E. Pastor, Y. Ma, A. Kafizas, T. E. Rosser, M. T. Mayer, E. Reisner, M. Grätzel, V. S. Batista, and J. R. Durrant, Nat. Chem. **12**, 82 (2019).

[12] K. U. Wijayantha, S. Saremi-Yarahmadi, and L. M. Peter, Phys. Chem. Chem. Phys. **13**, 5264 (2011).

[13] F. L. Formal, K. Sivula, and M. Grätzel, J. Phys. Chem. C **116**, 26707 (2012).

[14] G. Li, Y. Jin, Y. Yan, M. Wang, W. Tan, F. Liu, X. Feng, and H. Yin, Chem. Eng. J. **401**, 126124 (2020).

[15] A. Braun, K. Sivula, D. K. Bora, J. Zhu, L. Zhang, M. Grätzel, J. Guo, and E. C. Constable, J. Phys. Chem. C **116**, 16870 (2012).

[16] J. Zhang, Q. Lin, Z. Wang, H. Liu, and Y. Zhang, doi:10.26434/chemrxiv.14504955.v1.

[17] C. D. Bohn, A. K. Agrawal, E. C. Walter, M. D. Vaudin, A. A. Herzing, P. M. Haney, A. A. Talin, and V. A. Szalai, J. Phys. Chem. C **116**, 15290 (2012).

[18] C. M. Tian, W.-W. Li, Y. M. Lin, Z. Z. Yang, L. Wang, Y. G. Du, H. Y. Xiao, L. Qiao, J. Y. Zhang, L. Chen, D.-C. Qi, J. L. MacManus-Driscoll, and K. H. L. Zhang, J. Phys. Chem. C **124**, 12548 (2020).

[19] Z. Zhou, P. Huo, L. Guo, and O. V. Prezhdo, J. Phys. Chem. C **119**, 26303 (2015).

[20] A. Subramanian, E. Gracia-Espino, A. Annamalai, H. H. Lee, S. Y. Lee, S. H. Choi, and J. S. Jang, Appl. Surf. Sci. **427**, 1203 (2018).

[21] I. Cesar, A. Kay, J. A. G. Martinez, and M. Grätzel, J. Am. Chem. Soc. **128**, 4582 (2006).

[22] R. Mo, Q. Liu, H. Li, S. Yang, and J. Zhong, J. Mater. Sci.: Mater. Electron. **30**, 21444 (2019).

[23] P. Liao, M. C. Toroker, and E. A. Carter, Nano Lett. **11**, 1775 (2011).

[24] M. N. Huda, A. Walsh, Y. Yan, S.-H. Wei, and M. M. Al-Jassim, J. Appl. Phys. **107**, 123712 (2010).

[25] M. H. Lee, J. H. Park, H. S. Han, H. J. Song, I. S. Cho, J. H. Noh, and K. S. Hong, Int. J. Hydrogen Energy **39**, 17501 (2014).

[26] S. Ho-Kimura, B. A. D. Williamson, S. Sathasivam, S. J. A. Moniz, G. He, W. Luo, D. O. Scanlon, J. Tang, and I. P. Parkin, ACS Omega **4**, 1449 (2019).

[27] D. Ding, B. Dong, J. Liang, H. Zhou, Y. Pang, and S. Ding, ACS Appl. Mater. Interfaces **8**, 24573 (2016).

[28] A. Kay, D. A. Grave, D. S. Ellis, H. Dotan, and A. Rothschild, ACS Energy Lett. **1**, 827 (2016).

[29] G. Franceschi, F. Kraushofer, M. Meier, G. S. Parkinson, M. Schmid, U. Diebold, and M. Riva, Chem. Mater. **32**, 3753 (2020).

[30] H. Pan, X. Meng, D. Liu, S. Li, and G. Qin, Phys. Chem. Chem. Phys. **17**, 22179 (2015).

[31] K. Kang, H. Zhang, J. H. Kim, W. J. Byun, and J. S. Lee, Nanoscale Advances **4**, 1659 (2022).

[32] P. Biswas, A. Ainabayev, A. Zhussupbekova, F. Jose, R. O'Connor, A. Kaisha, B. Walls, and I. V. Shvets, Sci. Rep. **10**, 7463 (2020).

[33] B. Iandolo, B. Wickman, I. Zorić, and A. Hellman, J. Mater. Chem. A **3**, 16896 (2015).

[34] A. Shavorskiy, X. Ye, O. Karslıoğlu, A. D. Poletayev, M. Hartl, I. Zegkinoglou, L. Trotochaud, S. Nemšák, C. M. Schneider, E. J. Crumlin, S. Axnanda, Z. Liu, P. N. Ross, W. Chueh, and H. Bluhm, J. Phys. Chem. Lett. **8**, 5579 (2017).

[35] S. Chatman, C. I. Pearce, and K. M. Rosso, Chem. Mater. **27**, 1665 (2015).

[36] O. Zandi, A. R. Schon, H. Hajibabaei, and T. W. Hamann, Chem. Mater. **28**, 765 (2016).

[37] K. Zhang, T. Dong, G. Xie, L. Guan, B. Guo, Q. Xiang, Y. Dai, L. Tian, A. Batool, S. U. Jan, R. Boddula, A. A. Thebo, and J. R. Gong, ACS Appl. Mater. Interfaces **9**, 42723 (2017).

[38] J. P. Perdew, K. Burke, and M. Ernzerhof, Phys. Rev. Lett. **77**, 3865 (1996).

[39] V. I. Anisimov, J. Zaanen, and O. K. Andersen, Phys. Rev. B **44**, 943 (1991).

[40] P. Giannozzi, S. Baroni, N. Bonini, M. Calandra, R. Car, C. Cavazzoni, D. Ceresoli, G. L. Chiarotti, M. Cococcioni, I. Dabo, A. D. Corso, S. de Gironcoli, S. Fabris, G. Fratesi, R. Gebauer, U. Gerstmann, C. Gougoussis, A. Kokalj, M. Lazzeri, L. Martin-Samos, N. Marzari, F. Mauri, R. Mazzarello, S. Paolini, A. Pasquarello, L. Paulatto, C. Sbraccia, S. Scandolo, G. Sclauzero, A. P. Seitsonen, A. Smogunov, P. Umari, and R. M. Wentzcovitch, J. Phys.: Condens. Matter **21**, 395502 (2009).

[41] Z. D. Pozun and G. Henkelman, J. Chem. Phys. **134**, 224706 (2011).

[42] J. M. D. Coey and G. A. Sawatzky, J. Phys. C **4**, 2386 (1971).

[43] See Supplemental Material at http://link.aps.org/supplemental/10.1103/PhysRevMaterials.6.104604 for additional information.

[44] Y. Y. Avital, H. Dotan, D. Klotz, D. A. Grave, A. Tsyganok, B. Gupta, S. Kolusheva, I. Visoly-Fisher, A. Rothschild, and A. Yochelis, Nat. Commun. **9**, 4060 (2018).